Journal of Marine Science and Application (2019) 18:314–324
https://doi.org/10.1007/s11804-019-00095-5

RESEARCH ARTICLE

Applying Finite Difference Method to Simulate the Performance of a Perforated Breakwater Under Regular Waves

Javad Mohammadbagheri[1] · **Fouad Salimi**[2] · **Maryam Rahbani**[3]

Received: 3 November 2017 / Accepted: 18 November 2018 / Published online: 1 August 2019

Abstract

Using a discretized finite difference method, a numerical model was developed to study the interaction of regular waves with a perforated breakwater. Considering a non-viscous, non-rotational fluid, the governing equations of Laplacian velocity potential were developed, and specific conditions for every single boundary were defined. The final developed model was evaluated based on an existing experimental result. The evaluated model was used to simulate the condition for various wave periods from 0.6 to 2 s. The reflection coefficient and transmission coefficient of waves were examined with different breakwater porosities, wave steepnesses, and angular frequencies. The results show that the developed model can suitably present the effect of the structural and hydraulic parameters on the reflection and transmission coefficients. It was also found that with the increase in wave steepness, the reflection coefficient increased logarithmically, while the transmission coefficient decreased logarithmically.

Keywords Perforated breakwater · Transmission coefficient · Reflection coefficient · Numerical model · Finite difference method · Regular waves

1 Introduction

Since 1961 when Jarlan (1961) introduced the perforated breakwater, it has become popular in coastal areas all over the world. Ever since, researchers all around the world have proposed modifications and innovations of perforated breakwaters; among such, researchers are Suh et al. (2006), Liu et al. (2012a, b), Liu et al. (2015), and Elbisy (2017).

Article Highlights

- Discretized finite difference method used to develop governing equations for simulating transmission and reflection coefficients of perforated breakwater in interaction with regular waves.
- Results of simulations showed that in a perforated breakwater, increase in the porosity results in logarithmic increase and decrease in transmission and reflection coefficient, respectively.

According to Elbisy (2017), perforated breakwaters have gained extensive attraction compared to the previous breakwaters because it prevents the problem of wave reflection and scouring at the toe of breakwaters. Besides, the construction of these breakwaters can be very flexible; that is, the percentage of porosity, direction of perforation, and density of the wall can be modified with regard to any specific case. There are vast works on any of these parameters. For instance, Teng et al. (2004) and Dhinakaran et al. (2009) focused on breakwater porosity; Fugazza and Natale (1992) and Liu et al. (2007) investigated the design of perforation in breakwaters; and Teh et al. (2011) studied the stability of perforated breakwater as regards its density.

Since these structures are expensive to build and difficult to install, conducting a numerical study is necessary to calculate the efficiency of the structure and evaluate its performance for any designated area. This explains why numerical methods for simulating the performance of breakwaters are popular among scientists.

Finite difference, finite element, and finite volume methods can be applied to resolve a problem using numerical models. Among them, the finite difference method is defined dimension per dimension, which makes it useful for regular grids. In other words, if the geometry of a domain is rectangular and applicable for a regular grid, finite difference method will be a

✉ Maryam Rahbani
maryamrahbani@yahoo.com

[1] Department of Civil Engineering, Amirkabir University, Tehran 1134, Iran

[2] Department of Engineering, University of Hormozgan, Bandar Abbas 79131, Iran

[3] Department of Marine Science and Technology, University of Hormozgan, Bandar Abbas 79131, Iran

proper choice for numerical simulation, which is the case in this study.

Li et al. (2003) investigated the performance of a perforated breakwater under oblique waves with various incident angles. They employed the eigenfunction expansion method and compared their output results with the experimental results. They claimed that the water depth at the edge of the structure, the wavelength and height, and the dimension and porosity of the breakwater are the most effective parameters affecting the reflection coefficient of the wave.

In another investigation, Suh et al. (2006) used a numerical method to reveal the behavior of a perforated breakwater in front of a random wave. They argued that for regular waves, the minimum value for reflection coefficient can be reduced to 0, while for the random waves, this minimum value is about 0.3 to 0.4.

In an analytical research, Ketabdari and Varjavand (2008) studied the interaction between waves and perforated breakwater and reported that the increase in porosity caused an increase and decrease in transmission coefficient and reflection coefficient, respectively.

Furthermore, Liu et al. (2007) studied the hydrodynamic performance of a perforated breakwater under a regular wave, and they reported the advantages of implementing breakwater with a horizontal perforated structure as high capacity for dissipating wave energy and high stability.

Chen et al. (2011) employed Reynolds-averaged Navier-Stokes and K-L equations in a numerical model to estimate pressure on a perforated breakwater caused by random waves. In their study, the fluid was considered non-viscous and incompressible. They reported the effective parameters as mean water depth, wave steepness, percentage of porosity, and dimension of breakwater.

Following the research of Li et al. (2003), Koraim (2011) analytically investigated the effect of several parameters, which include transmission coefficient, reflection coefficient, and dissipation coefficient, on the performance of a perforated breakwater under a regular wave. He argued that the transmission coefficient decreases with increasing depth and wave steepness and decreasing porosity. Liu et al. (2012a, b) also studied the performance of a perforated breakwater under obliquely incident waves. They employed an infinite array of uniform multi-chamber perforated caissons with partition walls for their experiments and used the eigenfunction expansion method to develop their model. Both the periodicities of breakwater and the wave were incorporated into the solution they achieved. They claimed that perforated caissons with two or three uniform chambers could have a good wave absorption performance. Their results also indicated that the dimensionless horizontal force in the normal direction of the breakwater decreased with the increasing angle of incident waves.

2 Material and Methods

2.1 Numerical Model Development

Considering the general shape of a breakwater, the finite difference method was chosen for model development. To develop the model, the governing equations of Laplacian velocity potential are defined: logical assumptions to reduce the complexity of the equations are discussed; conditions for every single boundary are identified; the points with more than one boundary conditions are allocated; and finally, the proper equations applicable to the model are introduced. Figure 1 shows the schematic view of an analytical domain and its boundary conditions. The red line in the figure represents a breakwater.

Considering the general velocity potential as Eq. (1) and taking into account that the breakwater is fixed, the velocity potential of the radiated wave can be discarded; therefore, the format of Eq. (1) can be modified to that of eq. (2).

$$\phi = \phi_I + \phi_S + \phi_R \tag{1}$$

$$\phi = \phi_I + \phi_S \tag{2}$$

where ϕ_I, ϕ_S, and ϕ_r are the velocity potentials for incident, scattered, and radiated waves, respectively.

Considering small-amplitude waves and low celerity, some of the boundary conditions can be linearized, and the nonlinear parts can be eliminated. Equation (3) shows the linearized free surface boundary condition.

$$\frac{\partial^2 \phi}{\partial t^2} = -g\frac{\partial \phi}{\partial z} \Leftarrow \text{on } z = 0 \tag{3}$$

Equation (4) shows the relationship between wave celerity and potential velocity.

$$\frac{\partial \phi}{\partial n} = v(\boldsymbol{x}, t) \tag{4}$$

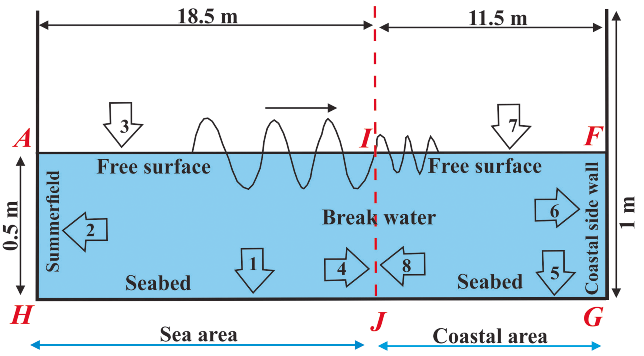

Fig. 1 Schematic view of the analytical domain

The bottom boundary condition can be derived from Eq. (4) as follows:

$$\frac{\partial\phi}{\partial z}=0 \tag{5}$$

At the bottom, the governed equation is $\frac{\partial\phi_I}{\partial z}=0$; Eq. (5) thus can be reduced to the following shape:

$$\frac{\partial\phi_s}{\partial z}=0 \tag{6}$$

The shore-side lateral boundary condition can be read as follows:

$$\frac{\partial\phi}{\partial x}=0 \tag{7}$$

As seen in Fig. 1, there are two more boundary conditions: far side boundary condition, which is known as Summerfeld, and boundary condition at the breakwater. These are further introduced in this section.

It should be noted that all the abovementioned equations are defined with the time domain. However, dealing with time complicates solving the equation. To eliminate this complexity, it is necessary to convert the equations into the frequency domain. For this reason, Eqs. (8) to (10) are employed.

$$\boldsymbol{q}=\boldsymbol{u}(\boldsymbol{x})\cdot\mathrm{e}^{-\mathrm{i}\omega t} \tag{8}$$

$$\xi=\eta(x,y)\cdot\mathrm{e}^{-\mathrm{i}\omega t} \tag{9}$$

$$\phi=\varphi(\boldsymbol{x})\cdot\mathrm{e}^{-\mathrm{i}\omega t} \tag{10}$$

The parameters on the left-hand side of the above equations are celerity vector, wave profile, and velocity potential, respectively. In the right-hand side, the $\mathrm{e}^{-\mathrm{i}\omega t}$ term is multiplied with the time-related terms to eliminate the time dependency of the equations (Banerjee and Wilson 2005).

Applying the three above equations, all the governing equations can be rewritten in the frequency domain. The parameters ϕ and ξ in the time domain equations are respectively replaced by φ and η in the frequency domain equations.

Eq. (2) also can be rewritten as follows:

$$\varphi=\varphi_I+\varphi_S \tag{11}$$

Considering Eq. (2), the free-surface boundary condition, which is a product of kinematic and dynamic boundary conditions, can be written in the frequency domain as follows:

$$\frac{\partial\varphi}{\partial z}=\frac{\omega^2}{g}\varphi \Leftarrow \text{on} \quad z=0 \tag{12}$$

Equations (6) and (7), the bottom and shore-side lateral boundary conditions, are converted respectively to Eqs. (13) and (14):

$$\frac{\partial\varphi_S}{\partial z}=0 \tag{13}$$

$$\frac{\partial\varphi}{\partial x}=0 \tag{14}$$

The lateral offshore boundary condition, known as Summerfeld, is as follows:

$$\frac{\partial\varphi_s}{\partial x}+i\cdot k\cdot\varphi_s=0 \tag{15}$$

As mentioned, the final boundary condition is for the situation at the breakwater itself. This condition can be written as follows:

$$\frac{\partial\varphi_1}{\partial x}=\frac{\partial\varphi_2}{\partial x}=i\cdot G(\varphi_1-\varphi_2) \tag{16}$$

where φ_1 and $\varphi_2$are velocity potentials at the breakwater toe in the seaside and shore side, respectively (see Fig. 1). Thus, the boundary condition at the breakwater can be divided into two parts: the boundary conditions at the seaside and at the shore side of the breakwater. They can be read as Eqs. (17) and (18), respectively.

$$\frac{\partial\varphi_s}{\partial x}+\frac{\partial\varphi_I}{\partial x}=i\cdot G\cdot(\varphi_s+\varphi_I-\varphi_2) \tag{17}$$

$$\frac{\partial\varphi_2}{\partial x}=i\cdot G(\varphi_s+\varphi_I-\varphi_2) \tag{18}$$

In the above equations, the coefficient G is defined as follows:

$$G=\frac{r}{b\,(f-i\cdot s)} \tag{19}$$

where r, b, f, and s are correspondingly the porosity, width, frictional coefficient, and inertial coefficient of the breakwater. The values of r, f, and s can be derived using Eqs. (20), (21), and (22), respectively, and b is derived from measurement (Suh et al. 2011). The width of the breakwater (b) is constant along with the breakwater height; therefore, it is not calculated in the modeling (see Fig. 3).

$$r=\frac{a}{A} \tag{20}$$

$$f=0.0584\left(\frac{r\cdot b}{h}\right)^{-0.7} \tag{21}$$

$$s=1-\frac{C_m\cdot(1-r)}{r} \tag{22}$$

In the above equations, C_m and h are additional mass coefficient and water depth, respectively. The value of C_m and s are considered as 0 and 1, respectively, in this study, which is also suggested by Suh et al. (2011) for perforated breakwater.

To develop a numerical model applicable for different geometrical and hydraulic conditions, the governing equations, along with the abovementioned boundary conditions, were considered and the finite difference method was applied. The developed numerical model is supposed to provide the reflection and transmission coefficients of the incident waves.

Eq. (23) is the discretized shape of the governing equation, considering finite difference method relations.

$$\frac{\partial^2\varphi}{\partial x^2}+\frac{\partial^2\varphi}{\partial y^2}=0\Rightarrow\frac{\varphi(i+1,j)+\varphi(i-1,j)-2\varphi(i,j)}{e_i^2}+ \frac{\varphi(i,j+1)+\varphi(i,j-1)-2\varphi(i,j)}{e_j^2}=0 \tag{23}$$

$$\Rightarrow A_1^2\cdot\varphi_s(i+1,j)+A_1^2\cdot\varphi_s(i-1,j)+\varphi_s(i,j+1)+ \varphi_s(i,j-1)-2\left(A_1^2+1\right)\cdot\varphi_s(i,j)=0$$

Here, $A_1=\frac{e_j}{e_i}$, where the numerator (e_j) represents the vertical distance between the two adjacent horizontal nodes, and denominator (e_i) represents the horizontal distance between the two adjacent vertical nodes.

To discretize different parts of the analytical domain in order to propose different equations applicable to each specific boundary, the boundaries of the domain are numbered 1 to 8, as seen in Fig. 2. Moreover, those points with more than one boundary condition are specified with the letters A, F, G, H, I, and J.

To use the finite difference method, the whole area should be meshed. The nodes, that is, the intersections of the vertical and horizontal meshes, within the area are the points for which the governing equations should be applied. It is important to note that those nodes located on the boundaries should be validated for all equations to be applied.

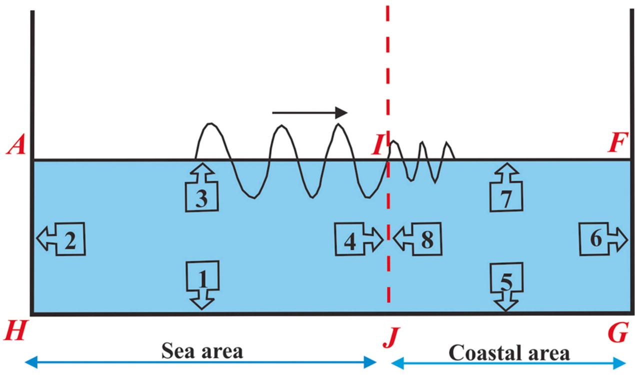

Fig. 2 Numerated boundary conditions of the analytical domain

The equations applicable to particular boundaries are presented hereafter. They are discretized using the finite difference method and taking into account the governed conditions at the considered boundary.

2.2 Boundary No. 1: Bottom Boundary–Offshore Side

$$\frac{\partial\varphi_s}{\partial z}=0\Rightarrow\frac{\varphi_s(i,j+1)-\varphi_s(i,j-1)}{2e_j}=0 \\ \Rightarrow\varphi_s(i,j-1)=\varphi_s(i,j+1) \tag{24}$$

Substituting Eq. (24) into Eq. (23) and rearranging the terms, the following is obtained:

$$A_1^2\cdot\varphi_s(i+1,j)+A_1^2\cdot\varphi_s(i-1,j)+2\varphi_s(i,j+1)- 2\left(A_1^2+1\right)\cdot\varphi_s(i,j)=0 \tag{25}$$

2.3 Boundary No. 2: Lateral Boundary–Offshore Side (Summerfeld)

$$\frac{\partial\varphi_s}{\partial x}=-i\cdot k\cdot\varphi_s \\ \Rightarrow\frac{\varphi_s(i+1,j)-\varphi_s(i-1,j)}{2e_i}=-i\cdot k\cdot\varphi_s(i,j) \\ \Rightarrow\varphi_s(i-1,j)=\varphi_s(i+1,j)+j(2k\cdot e_i)\cdot\varphi_s(i,j) \tag{26}$$

Substituting Eq. (26) into Eq. (23) and rearranging the terms, Eq. (27) can be derived.

$$2A_1^2\cdot\varphi_s(i+1,j)+\varphi_s(i,j+1)+\varphi_s(i,j-1) -\left[2\left(A_1^2+1\right)-i\left(2A_1^2\cdot k\cdot e_i\right)\right]\cdot\varphi_s(i,j)=0 \tag{27}$$

2.4 Boundary No. 3: Free-Surface–Offshore Side

$$\frac{\omega^2}{g}\cdot\varphi_s=\frac{\partial\varphi_2}{\partial z}\Rightarrow A_2\cdot\varphi_s(i,j)=\frac{\varphi_s(i,j+1)-\varphi_s(i,j-1)}{2e_j} \\ \Rightarrow 2A_2\cdot e_j\cdot\varphi_s(i,j)=\varphi_s(i,j+1)-\varphi_s(i,j-1) \tag{28}$$

Substituting Eq. (28) into the governing equation results in the following:

$$A_1^2\cdot\varphi_s(i+1,j)+A_1^2\cdot\varphi_s(i-1,j)+2\varphi_s(i,j-1)- \left[2\left(A_1^2+1\right)-\left(2A_2.e_j\right)\right]\cdot\varphi_s(i,j)=0 \tag{29}$$

(where) $A_2=\frac{\omega^2}{g}$

2.5 Boundary No. 4: Breakwater Boundary–Seaside

$$\begin{gathered}\frac{\partial\varphi_1}{\partial x}=i\cdot G\cdot(\varphi_1-\varphi_2)\Rightarrow\frac{\partial\varphi_s}{\partial x}+\frac{\partial\varphi_I}{\partial x}=i\cdot G\cdot(\varphi_s+\varphi_I-\varphi_2)\\ \Rightarrow\frac{\varphi_s(i+1,j)-\varphi_s(i-1,j)}{2e_i}=iG(\varphi_s+A_4-\varphi_2)-A_3\\ \Rightarrow\varphi_s(i+1,j)=\varphi_s(i-1,j)+\\ i[2G\cdot e_i(\varphi_s(i,j)+A_4-\varphi_2(i,j))]-2A_3\cdot e_i\end{gathered}\tag{30}$$

Employing the same procedure as those of previous boundaries, Eq. (30) can be rewritten as follows:

$$\begin{gathered}2A_1^2\cdot\varphi_s(i-1,j)+\varphi_s(i,j+1)+\varphi_s(i,j-1)+\\ 2\left[i\left(A_1^2\cdot G\cdot e_i\right)-\left(A_1^2+1\right)\right]\cdot\varphi_s(i,j)-\\ i\left(2A_1^2\cdot G\cdot e_i\right).\varphi_2(i,j)=\\ -i\left(2A_1^2\cdot A_4\cdot G\cdot e_i+2A_1^2\cdot A_3\cdot e_i\right)\end{gathered}\tag{31}$$

where $A_3=\frac{\partial\varphi_I}{\partial x}=\frac{g.k.H_i}{2\omega}\cdot\frac{Cosh[k(z+h)]}{Cosh(k.h)}\cdot e^{i.k.x}$ and $A_4=\varphi_I=\frac{-i.g.H_i}{2\omega}\cdot\frac{Cosh[k(z+h)]}{Cosh(k.h)}\cdot e^{i.k.x}$.

2.6 Boundary No. 5: Bottom Boundary–Shore Side

$$\begin{gathered}\frac{\partial\varphi_2}{\partial z}=0\Rightarrow\frac{\varphi_2(i,j+1)-\varphi_2(i,j-1)}{2e_j}=0\\ \Rightarrow\varphi_2(i,j-1)=\varphi_2(i,j+1)\end{gathered}\tag{32}$$

which can be rewritten as follows:

$$\begin{gathered}A_1^2\cdot\varphi_2(i+1,j)+A_1^2\cdot\varphi_2(i-1,j)+\\ 2\varphi_2(i,j+1)-2\left(A_1^2+1\right)\cdot\varphi_2(i,j)=0\end{gathered}\tag{33}$$

2.7 Boundary No. 6: Lateral Boundary–Shore Side

$$\begin{gathered}\frac{\partial\varphi_2}{\partial x}=0\Rightarrow\frac{\varphi_2(i+1,j)-\varphi_2(i-1,j)}{2e_i}=0\\ \Rightarrow\varphi_2(i+1,j)=\varphi_2(i-1,j)\end{gathered}\tag{34}$$

Eq. (35) is the result of substituting Eq. (34) into Eq. (23).

$$\begin{gathered}2A_1^2\cdot\varphi_2(i-1,j)+\varphi_2(i,j+1)+\\ \varphi_2(i,j-1)-2\left(A_1^2+1\right)\cdot\varphi_2(i,j)=0\end{gathered}\tag{35}$$

2.8 Boundary No. 7: Free-Surface–Shore Side

$$\begin{gathered}\frac{\omega^2}{g}\cdot\varphi_2=\frac{\partial\varphi_2}{\partial z}\Rightarrow A_2\cdot\varphi_2(i,j)=\frac{\varphi_2(i,j+1)-\varphi_2(i,j-1)}{2e_j}\\ \Rightarrow 2A_2\cdot e_j\cdot\varphi_2(i,j)=\varphi_2(i,j+1)-\varphi_2(i,j-1)\\ \Rightarrow\varphi_2(i,j+1)=2e_j\cdot A_2\cdot\varphi_2(i,j)+\varphi_2(i,j-1)\end{gathered}\tag{36}$$

Applying the same procedure, the equation becomes as follows:

$$\begin{gathered}A_1^2\cdot\varphi_2(i+1,j)+A_1^2\cdot\varphi_2(i-1,j)+\\ 2\varphi_2(i,j-1)-\left[2\left(A_1^2+1\right)-\left(2A_2.e_j\right)\right]\cdot\varphi_2(i,j)=0\end{gathered}\tag{37}$$

2.9 Boundary No. 8: Breakwater Boundary–Shore Side

$$\begin{gathered}\frac{\partial\varphi_2}{\partial x}=i\cdot G(\varphi_1-\varphi_2)\Rightarrow\frac{\partial\varphi_2}{\partial x}=i\cdot G(\varphi_s+\varphi_i-\varphi_2)\\ \Rightarrow\frac{\varphi_2(i+1,j)-\varphi_2(i-1,j)}{2e_i}=i\cdot G(\varphi_s+A_4-\varphi_2)\\ \Rightarrow\varphi_2(i-1,j)=\varphi_2(i+1,j)-\\ i[2G\cdot e_i(\varphi_s(i,j)+A_4-\varphi_2(i,j))]\end{gathered}\tag{38}$$

Substituting Eq. (38) into Eq. (23), the following is obtained:

$$\begin{gathered}2A_1^2\cdot\varphi_2(i+1,j)+\varphi_2(i,j+1)+\varphi_2(i,j-1)+\\ 2\left[i\left(A_1^2\cdot G\cdot e_i\right)-\left(A_1^2+1\right)\right]\cdot\varphi_2(i,j)-\\ i\left(2A_1^2\cdot G\cdot e_i\right)\cdot\varphi_s(i,j)=i\left(2A_1^2\cdot A_4\cdot G\cdot e_i\right)\end{gathered}\tag{39}$$

To this point, all equations representing the conditions for the eight specified boundaries (see Fig. 2) have been introduced. Hereafter, equations indicating the condition of those nodes located at the interface of two incident boundaries are presented.

2.10 Boundary at Point A

Considering the interface of boundaries No. 2 and No. 3, by substituting Eqs. (26) and (28) into the governing equation of Eq. (23) and rearranging the terms, the following equation can be derived:

$$\begin{gathered}2A_1^2\cdot\varphi_s(i+1,j)+2\varphi_s(i,j-1)+\\ \left[i\left(2k\cdot A_1^2\cdot e_i\right)+2e_j\cdot A_2-2\left(A_1^2+1\right)\right]\cdot\varphi_s(i,j)=0\end{gathered}\tag{40}$$

2.11 Boundary at Point F

Point F is located at the interface of boundaries no. 6 and no. 7. Therefore, Eqs. (34) and (36) are applied to the main Eq. (23) to derive Eq. (41).

$$2A_1^2\cdot\varphi_2(i-1,j)+2\varphi_2(i,j-1)+\left[2A_2\cdot e_j-2\left(A_1^2+1\right)\right]\varphi_2(i,j)=0\tag{41}$$

2.12 Boundary at Point G

Point G is at the interface of boundaries no. 5 and no.6. Therefore, Eqs. (32) and (34) are applied to Eq. (23) to obtain the following equation:

$$2A_1^2\cdot\varphi_2(i,-1,j)+2\varphi_2(i,j+1)-2\left(A_1^2+1\right)\cdot\varphi_2(i,j)=0 \tag{42}$$

2.13 Boundary at Point H

Point H is at the interface of boundaries No. 1 and No. 2. The Eqs. (24) and (26) are therefore substituted into Eq. (23).

$$\begin{aligned}&2A_1^2\cdot\varphi_s(i+1,j)+2\varphi_s(i,j+1)+\\&\left[j\left(2A_1^2\cdot k\cdot e_i\right)-2\left(A_1^2+1\right)\right]\cdot\varphi_s(i,j)=0\end{aligned} \tag{43}$$

2.14 Boundary at Point I

As seen in Fig. 2, this point can be considered as both seaside and shore side. Thus, two different equations should be developed for this point.

For the seaside part, boundaries No. 3 and No. 4 are interposed; therefore, Eqs. (28) and (30) are applied to Eq. (23) to give the following:

$$\begin{aligned}&2A_1^2\cdot\varphi_s(i-1,j)+2\varphi_s(i,j-1)+\Big[i\left(2A_1^2\cdot G\cdot e_i\right)+\\&2A_2e_j-2\left(A_1^2+1\right)\Big]\cdot\varphi_s(i,j)-i\left(2A_1^2\cdot G\cdot e_i\right)\cdot\varphi_2(i,j)=\\&-i\left(2A_1^2\cdot A_4\cdot G\cdot e_i\right)+2A_1^2\cdot A_3\cdot e_i\end{aligned} \tag{44}$$

For the shore side, however, boundaries No. 7 and No. 8 are interposed; therefore, Eqs. (36) and (38) are applied to derive Eq. (45).

$$\begin{aligned}&2A_1^2\cdot\varphi_2(i+1,j)+2\varphi_2(i,j-1)+\Big[i\left(2A_1^2\cdot G\cdot e_i\right)-\\&2\left(A_1^2+1\right)+2e_j\cdot A_2\Big]\cdot\varphi_2(i,j)-i\left(2A_1^2\cdot G\cdot e_i\right)\cdot\varphi_s(i,j)=\\&i\left(2A_1^2\cdot A_4\cdot G\cdot e_i\right)\end{aligned} \tag{45}$$

2.15 Boundary at Point J

Point J, being as point I, should also be considered as seaside and shore side. At the seaside, boundaries no. 1 and no. 4 are interposed; therefore, Eqs. (24) and (30) are substituted into Eq. (23) to obtain the following equation:

$$\begin{aligned}&2A_1^2\cdot\varphi_s(i-1,j)+2\varphi_s(i,j+1)+\Big[i\left(2A_1^2\cdot G\cdot e_i\right)-\\&2\left(A_1^2+1\right)\Big]\cdot\varphi_s(i,j)-i\left(2A_1^2\cdot G\cdot e_i\right)\cdot\varphi_2(i,j)=\\&2A_1^2\cdot A_3\cdot e_i-i\left(2A_1^2\cdot A_4\cdot G\cdot e_i\right)\end{aligned} \tag{46}$$

At the shore side, point J interposes boundaries no. 5 and no. 8; thus, Eqs. (32) and (38) are substituted into Eq. (23) to give the following:

$$\begin{aligned}&2A_1^2\cdot\varphi_2(i+1,j)+2\varphi_2(i,j+1)+\Big[i\left(2A_1^2\cdot G\cdot e_i\right)-\\&2\left(A_1^2+1\right)\Big]\cdot\varphi_2(i,j)-i\left(2A_1^2\cdot G\cdot e_i\right)\cdot\varphi_s(i,j)a=\\&i\left(2A_1^2\cdot A_4\cdot G\cdot e_i\right)\end{aligned} \tag{47}$$

The aim of this research is to obtain reflection and transmission coefficients. It is, therefore, necessary to overview the relationships employed in the model. Considering Bernoulli Eq. (48), Eq. (49) can be derived, which shows the height of crossed wave (height of water level) from the breakwater.

$$\frac{\partial\varphi}{\partial t}+\frac{1}{2}\left[\left(\frac{\partial\varphi}{\partial x}\right)^2+\left(\frac{\partial\varphi}{\partial z}\right)^2\right]+g\eta=C\rightarrow z=\eta(x,t) \tag{48}$$

$$\xi=\frac{\frac{\partial\phi}{\partial t}}{-g} \tag{49}$$

The ratio of maximum crossed wave height (ξ) to the initial wave height (H_i) is known as the transmission coefficient.

$$C_t=\frac{\max(\xi_1)}{H_i} \tag{50}$$

Considering a non-viscous and non-rotational fluid, the relationship between the reflection and transmission coefficients is as follows:

$$C_r=1-C_t \tag{51}$$

All the required equations have been obtained and can now be implemented in the model.

2.16 Experimental Investigation for Evaluating Numerical Model

To evaluate the developed numerical model, the results of the experimental study conducted by Suh et al. (2011) were used. The experiments were conducted in the Department of Civil and Environmental Engineering at Seoul National University. They used a wave flume with dimensions 30, 0.6, and 1 m, which was equipped with a wave maker at one side of it. They inserted the constructed breakwater in the flume, at the distance of 18.5 m from the wave maker. At the other side of the flume, a vertical plain wall was installed. The thickness of the breakwater was suggested to be between 2 and 3 cm. They conducted several experiments with various water levels, ranging from 30 to 70 cm. The experiments were conducted in time intervals of 1 to 2 s with a time step of 0.2 s and wave steepness of 0.03 (Suh et al. 2011).

Considering a as a half of the groove width and A as the half of the interval between the centers of two adjacent pile (Fig. 3), the porosity (r_0) of the breakwater was calculated as follows:

$$r_0 = \frac{2a}{2A} \tag{52}$$

The results reported by Suh et al. (2011) were used to evaluate the results derived from the developed numerical model.

3 Results and Discussions

3.1 Numerical Model Evaluation

The dimension of the flume in the numerical model was exactly the same as that in the experimental case. The depth was set to 50 cm, and the thickness, porosity, and friction coefficient of the breakwater were set to 4 cm, 0.4, and 0.6, respectively. Simulations were conducted for the periods between 0.6 and 2 s. Here, the studied waves were supposed as deep water waves, which means every period represents a specific wavelength, and thus a specific wave number.

The developed numerical model was then used to simulate the actual conditions and provide the transmission coefficient (C_t) and reflection coefficient (C_r) for each simulation. To evaluate the performance of the model, the simulation results were compared with the experimental results by Suh et al. (2011). In all simulations, the optimum grid size provided by Mohammadbagheri (2013) was used; that is, grids with length and width of 0.005 m. Statistical parameters that show the reliability of the simulations conducted using these grid values are presented in Table 1.

Figures 4 and 5 respectively present the transmission and reflection coefficients derived from the experimental tests and the numerical model. The coefficients were plotted against Kh, where K is wave number and h is depth. The plotted results show that the developed numerical model could effectively predict both transmission and reflection coefficients.

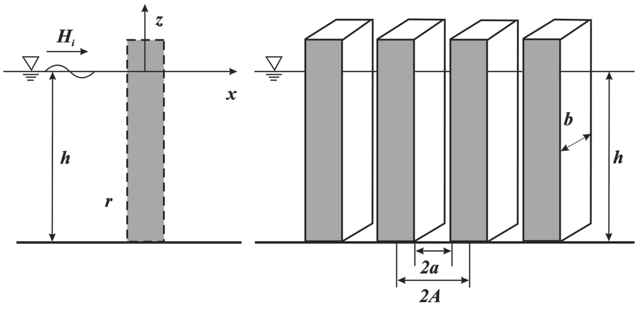

Fig. 3 Schematic view of piles and the intervals (Suh et al. 2011)

Table 1 The accuracy of the developed model based on statistical parameters

Statistical parameters	C_r	C_t
RMSE	0.028	0.028
SI	0.179	0.033
Bias	0.022	− 0.022
CC	0.978	0.978

The transmission coefficients derived from the model and experimental tests were in good agreement for all Kh (Fig. 4), while the correlation between the reflection coefficients (Fig. 5) was not as good as that between the transmission coefficients. This is because a non-frictional condition was considered for the modeling (Eq. (51)), while in the experimental tests, normal dissipation due to friction existed and non-frictional condition was not easily applicable. For such a condition where dissipation exists, according to Pérez-Romero et al. (2009) and Zhu (2011), the relationship between the reflection coefficient and transmission coefficient is calculated as follows:

$$D_* = 1 - C_r^2 - C_t^2 \tag{53}$$

where D_* is a dimensionless parameter representing dissipation due to friction. Considering the deviation between Eqs. (51) and (53), higher reflection coefficient values are expected from the model, compared with those of the experimental tests, as clearly seen in Fig. 5.

Figure 5 also shows that the deviation between the model and experimental results increased with the

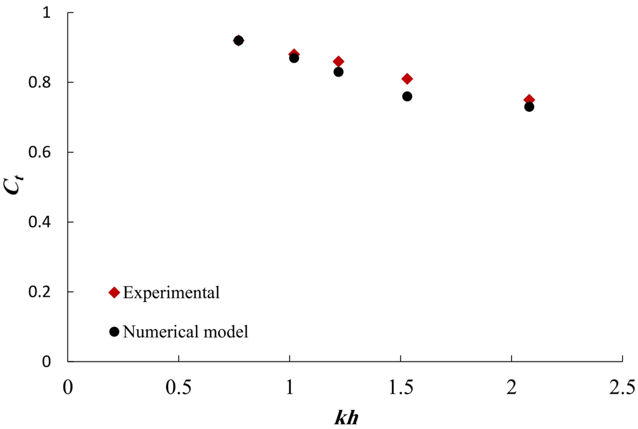

Fig. 4 Diagram of transmission coefficient versus Kh: a comparison between the results derived by Suh et al. (2011) and those of the developed numerical model

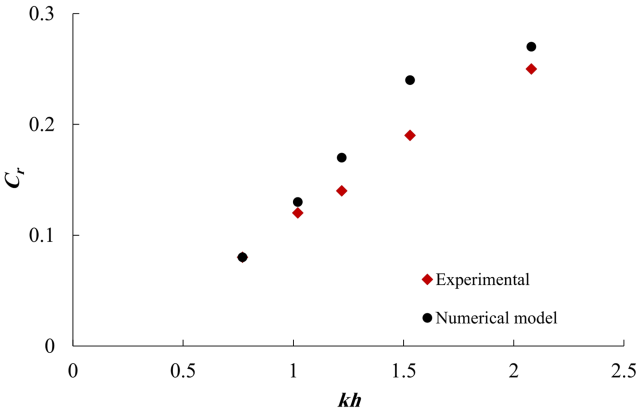

Fig. 5 Diagram of reflection coefficient versus *Kh*: a comparison between the results derived by Suh et al. (2011) and those of the developed numerical model

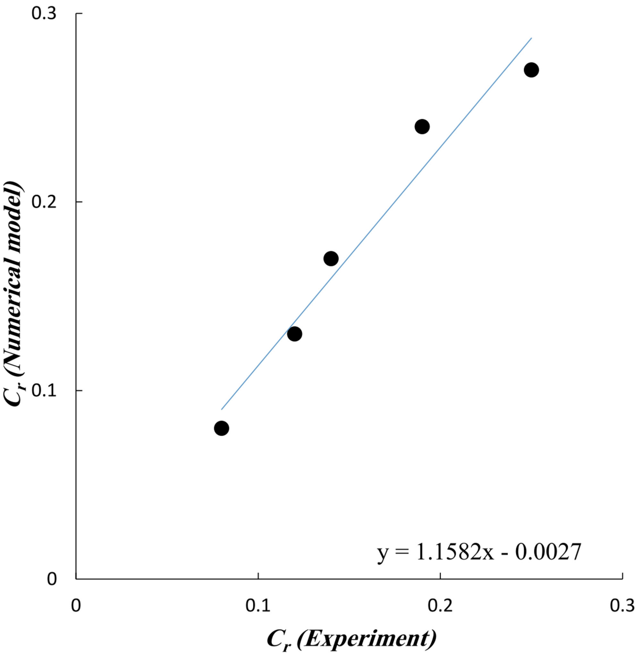

Fig. 7 Scatter diagram of reflection coefficients derived from the experimental tests by Suh et al. (2011) and the developed numerical model

increase in *Kh*. This is because an increase in *k* means an increase in the number of waves, which could cause an increase in friction, and thus an increase in D_* (Eq. (53)). Since the friction is not considered in the model, this deviation increases with increase in *Kh*.

Furthermore, it was seen that a major deviation occurred at *Kh* = 1.5. This could be explained considering the width of the breakwater (*b*). Several researchers, including Hales (1981), Ruey-Syan Shih (2012), and Lee and Jung (2018), have demonstrated that the ratio of width to wavelength is an important governing factor. In this research, the depth (*d*) was 50 cm; thus, the wave number (*k*) could be calculated as 3, which results in a wavelength (*L*) value of 2.09 cm. The width in the experimental test was 4 cm, which means the ratio of width to wavelength (*b*/*L*) in the study was 1.92. Hales (1981) in his research noted that for effective wave attenuation (highest dissipation due to friction), the width of the breakwater should be twice the wavelength (*b*/*L* = 2). This might be the situation in the experimental tests due to the friction; thus, the deviation between the experimental results and modeled data increased for the *Kh* value of 1.5.

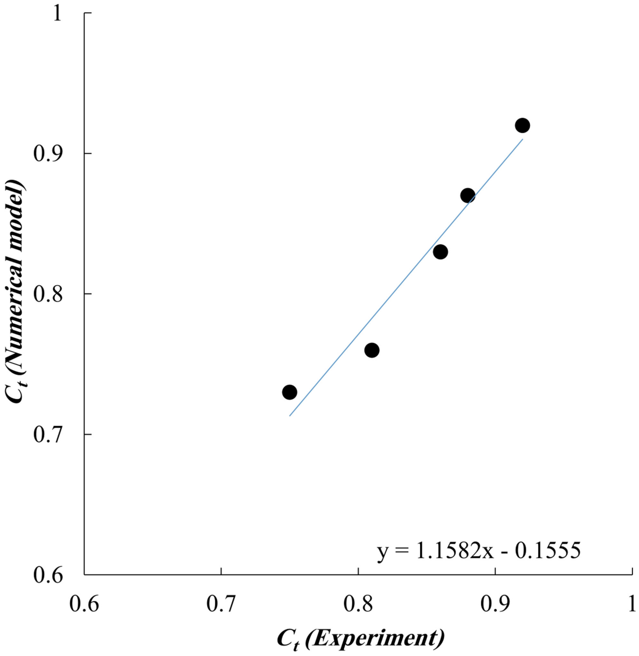

Fig. 6 Scatter diagram of transmission coefficients derived from the experimental tests by Suh et al. (2011) and the developed numerical model

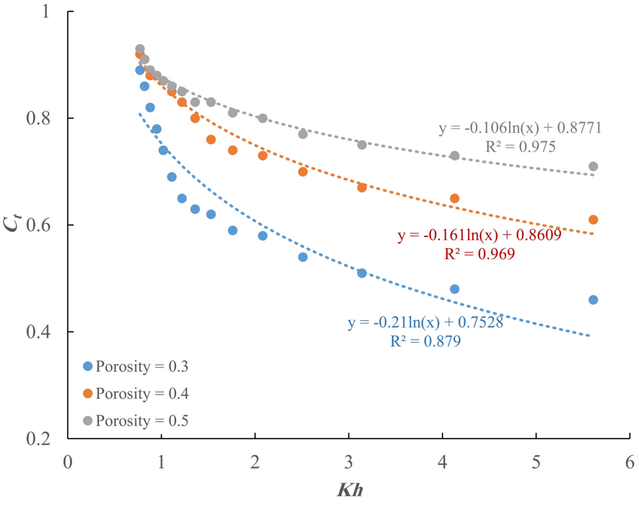

Fig. 8 Variation of transmission coefficient with *Kh* for different breakwater porosities of 0.3, 0.4, and 0.5

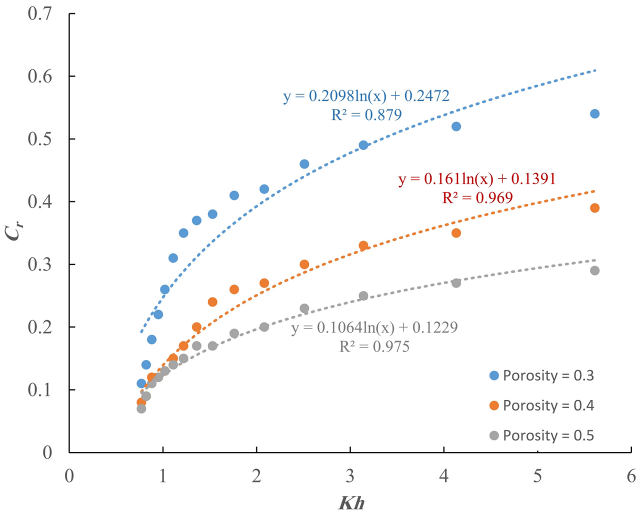

Fig. 9 Variation of reflection coefficient with *Kh* for different breakwater porosities of 0.3, 0.4, and 0.5

To statistically estimate the accuracy of the results derived from the numerical model, the relative mean square error (RMSE) and scatter index (SI) were employed (Eqs. (54) and 55). The bias parameter and correlation coefficient (CC) were also calculated (Eqs. (56) and (57)). For the transmission and reflection coefficients, these parameters are presented in Table 1. It can be seen that the results of the model agreed well with those of the experimental investigation.

$$\mathrm{RMSE} = \sqrt{\frac{1}{n}\sum(Y_i - X_i)^2} \tag{54}$$

$$\mathrm{SI} = \frac{\sqrt{\frac{1}{n}\sum\left(\left(Y_i - \overline{Y}\right) - \left(X_i - \overline{X}\right)\right)^2}}{\overline{X}} \tag{55}$$

$$\mathrm{Bias} = \left(\overline{Y} - \overline{X}\right) \tag{56}$$

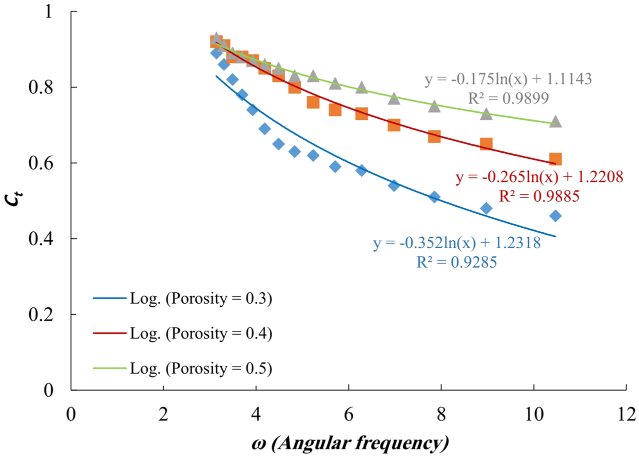

Fig. 10 Variation of transmission coefficient with angular frequency (ω) for different breakwater porosities of 0.3, 0.4, and 0.5

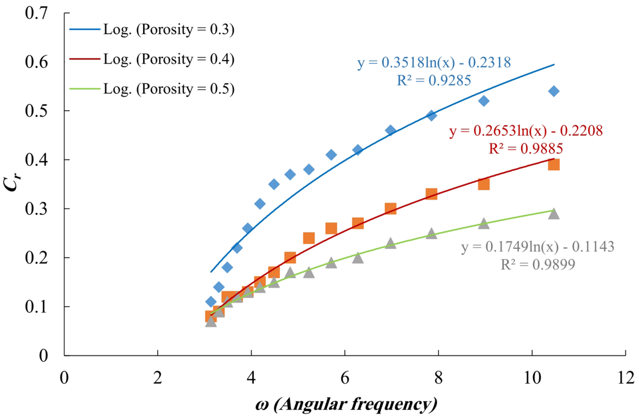

Fig. 11 Variation of reflection coefficient with angular frequency (ω) for different breakwater porosities of 0.3, 0.4, and 0.5

$$\mathrm{CC} = \frac{\sum\left(X_i - \overline{X}\right)\left(Y_i - \overline{Y}\right)}{\sqrt{\sum\left(X_i - \overline{X}\right)^2 \sum\left(Y_i - \overline{Y}\right)^2}} \tag{57}$$

Figures 6 and 7 show the scatter diagram of the transmission and reflection coefficients derived from the experimental tests of Suh et al. (2011) and the developed numerical model, respectively. Both figures show a reasonable correlation between the model results and the experimental results by Suh et al. (2011).

3.2 Performance of the Numerical Model with Various Porosity Values

Several experiments were conducted to study the variation of transmission coefficient and reflection coefficient with *Kh* for different porosities of 0.3, 0.4, and 0.5. The results for transmission and reflection coefficients are presented in Figs. 8 and 9, respectively.

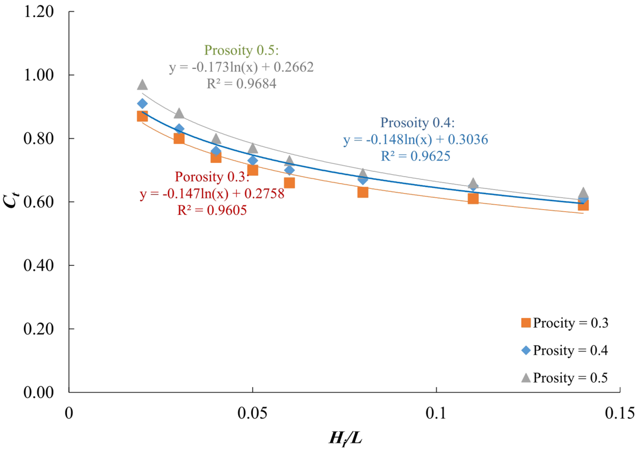

Fig. 12 Variation of transmission coefficient with wave steepness for different porosity values of 0.3, 0.4, and 0.5

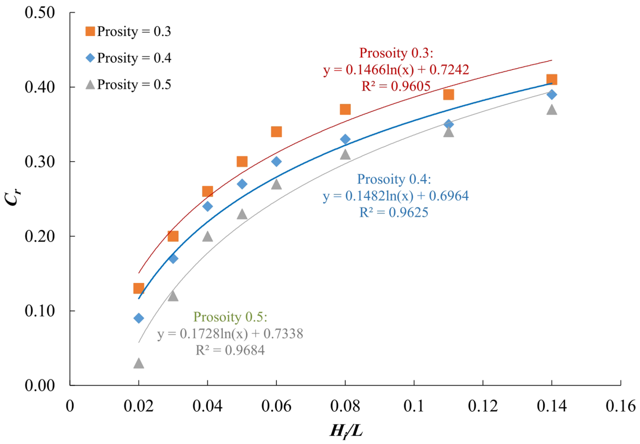

Fig. 13 Variation of reflection coefficient with wave steepness for different porosity values of 0.3, 0.4, and 0.5

Figure 8 shows that with the increase in *Kh*, transmission coefficient logarithmically decreased. It can also be seen that the increase in the breakwater porosity caused an increase in transmission coefficient. Figure 9, on the other hand, shows that with an increase in *Kh*, the reflection coefficient logarithmically increased. Moreover, an increase in porosity caused a decrease in reflection coefficient. The figures also demonstrate that the variation of both coefficients with *Kh* can be well predicted with a logarithmic fitting curve ($R^2 > 0.87$).

Furthermore, in both Figs. 8 and 9, a steep slope of variation for both coefficients (and for all porosities) can be observed up to the value $Kh = 2$; afterward, the slope smoothens. This variation trend was also observed and reported by Dalrymple et al. (1991).

The effects of angular frequency variation on the transmission and reflection coefficients were also examined considering different breakwater porosities. Figures 10 and 11 show the results for the transmission and reflection coefficients, respectively.

According to Fig. 10, increase in angular frequency caused a decrease in the transmission coefficient for all the perforated breakwaters. Figure 11 also shows that for all porosities, the increase in angular frequency caused an increase in reflection coefficient. In addition, the variation of both coefficients with angular frequency can be precisely presented by a logarithmic fitting curve.

In both Figs. 10 and 11, it can be seen that the coefficients variation trend exhibits a steep slope for periods higher than 1.25 s and a gentle slope for the periods below this value.

3.3 Relationship Between the Steepness and Breakwater Coefficients

Figures 12 and 13 present the effects of wave steepness variation on the transmission and reflection coefficients, respectively, for different porosities of 0.3, 0.4, and 0.5. As it is presented in the figures, the increase in wave steepness caused a decrease in transmission coefficient (Fig. 12) and an increase in the reflection coefficient (Fig. 13) for all porosities. By obtaining the best fitting curves for the data (Figs. 12 and 13), it was found that transmission and reflection coefficients varied logarithmically with the wave steepness. The relevant best fitting curve equations and coefficient of correlation (R^2) are presented in Table 2.

The results presented in Table 2 show that the best fitting curves and coefficients of correlation for porosities 0.3 and 0.4 are almost similar, and one single equation can be used to correlate wave steepness with reflection and transmission coefficients for both porosities. For the porosity 0.5, however, the equations are relatively different, and the coefficients of correlation for both reflection and transmission coefficients are slightly improved.

The coefficient of correlation values of 0.96 and 0.97 for the best fitting curves of transmission and reflection coefficients for all porosities prove the close logarithmic correlation between the steepness and the respective coefficients.

Thomson (2000) and Gous (2014) also reported a logarithmic correlation between the transmission coefficient and wave steepness. Hoolihalli and Hegde (2013), on the other hand, reported an exponential correlation between these two parameters.

It should, therefore, be emphasized that the curves and functions presented here are valid only for similar input parameters, and they may not be applicable to other values of the test parameters.

Table 2 Best fitting curve and coefficient of determination

Porosity	Reflection coefficient (C_r)		Transmission coefficient (C_t)	
	Best fitting curve	R^2	Best fitting curve	R^2
0.3	$C_r = 0.15\ln\left(\frac{H_i}{L}\right) + 0.72$	0.96	$C_t = -0.15\ln\left(\frac{H_i}{L}\right) + 0.28$	0.96
0.4	$C_r = 0.15\ln\left(\frac{H_i}{L}\right) + 0.70$	0.96	$C_t = -0.15\ln\left(\frac{H_i}{L}\right) + 0.30$	0.96
0.5	$C_r = 0.17\ln\left(\frac{H_i}{L}\right) + 0.73$	0.97	$C_t = -0.17\ln\left(\frac{H_i}{L}\right) + 0.27$	0.97

4 Conclusion

Using a discretized finite difference method, a numerical model was developed to simulate the performance of a simple breakwater under a regular wave. The developed model was evaluated based on an existing experimental investigation. The following results were obtained:

1 At a specific depth, the increase in the *Kh* resulted in a decrease in transmission coefficient and an increase in the reflection coefficient. This variation trend followed a logarithmic fitting curve. It was specifically steep for the *Kh* values between 0.77 and 1.36.
2 As the value of porosity increased, the transmission coefficient increased and the reflection coefficient decreased. The best fitting curves for both were logarithmic.
3 The increase in the angular frequency caused a decrease in transmission coefficient and an increase in the reflection coefficient.
4 The transmission coefficient logarithmically decreased with the increase of wave steepness. On the other hand, reflection coefficient logarithmically increased with wave steepness.
5 The transmission coefficients predicted by the developed model agreed better with those of the experimental results, compared with the reflection coefficients. This is because the model was not capable of simulating dissipation caused by friction.

References

Banerjee PK, Wilson B (2005) Developments in boundary element methods: industrial applications (vol. 5). CRC Press, USA, p 311

Chen X, Li Y, Long L (2011) Simulation of irregular wave pressure on perforated breakwaters. Coastal Engineering Proceedings 1(32):29. https://doi.org/10.9753/icce.v32.structures.29

Dalrymple RA, Losada MA, Martin PA (1991) Reflection and transmission from porous structures under oblique wave attack. J Fluid Mech 224:625–644

Dhinakaran G, Sundar V, Sundaravadivelu R, Graw KU (2009) Effect of perforations and rubble mound height on wave transformation characteristics of surface piercing semicircular breakwaters. Ocean Eng 36(15):1182–1198. https://doi.org/10.1016/j.oceaneng.2009.08.005

Elbisy MS (2017) Wave interactions with multiple semi-immersed Jarlan-type perforated breakwaters. China Ocean Engineering 31(3):341–349. https://doi.org/10.1007/s13344-017-0040-3

Fugazza M, Natale L (1992) Hydraulic design of perforated breakwaters. Journal of Waterway, Port, Coastal, and Ocean Engineering 118(1): 1–14. https://doi.org/10.1061/(ASCE)0733-950X(1992)118:1(1)

Gous W (2014) *Configurations of a piled row breakwater for a protected shallow water marina,* M.Sc thesis, Stellenbosch: Stellenbosch University, 135. http://hdl.handle.net/10019.1/86710

Hales LZ (1981) *Floating Breakwaters: State-of-the-Art Literature Review* (No. CERC-TR-81-1). COASTAL ENGINEERING RESEARCH CENTER FORT BELVOIR VA

Hoolihalli MV, Hegde AV (2013) Transmission studies on horizontal interlaced multi-layer moored floating pipe breakwater (HIMMFPB) with three layers of pipes. Indian Journal of Geo-Marine Sciences 42(6):722–728 http://nopr.niscair.res.in/handle/123456789/24802

Jarlan GE (1961) A perforated vertical wall breakwater. The Dock and Harbour Authority 486:394–398

Ketabdari MJ, Varjavand I (2008) Reflected energy spectrum from slotted breakwaters due to irregular waves. J Coast Res:1529–1535. https://doi.org/10.2112/06-0753.1

Koraim AS (2011) Hydrodynamic characteristics of slotted breakwaters under regular waves. J Mar Sci Technol 16(3):331–342. https://doi.org/10.1007/s00773-011-0126-1

Lee C, Jung TH (2018) Extended Boussinesq equations for waves in porous media. Coast Eng 139:85–97. https://doi.org/10.1016/j.coastaleng.2018.04.023

Li Y, Dong G, Liu H, Sun D (2003) The reflection of oblique incident waves by breakwaters with double-layered perforated wall. Coast Eng 50(1):47–60. https://doi.org/10.1016/j.coastaleng.2003.08.001

Liu Y, Li YC, Teng B (2007) Wave interaction with a perforated wall breakwater with a submerged horizontal porous plate. Ocean Eng 34(17):2364–2373. https://doi.org/10.1016/j.oceaneng.2007.05.002

Liu Y, Li YC, Teng B (2012a) Interaction between obliquely incident waves and an infinite array of multi-chamber perforated caissons. J Eng Math 74(1):1–18. https://doi.org/10.1007/s10665-011-9484-2

Liu J, Lin G, Li J (2012b) Short-crested waves interaction with a concentric cylindrical structure with double-layered perforated walls. Ocean Eng 40:76–90. https://doi.org/10.1016/j.oceaneng.2011.12.011

Liu Y, Yao ZL, Li HJ (2015) Analytical and experimental studies on hydrodynamic performance of semi-immersed Jarlan-type perforated breakwaters. China Ocean Engineering 29(6):793–806. https://doi.org/10.1007/s13344-015-0056-5

Mohammadbagheri J (2013) Finite difference numerical modeling for simulating the interaction of waves and breakwaters, MSc. Thesis, Amirkabir University of Technology, Iran. (in Persian)

Pérez-Romero DM, Ortega-Sánchez M, Moñino A, Losada MA (2009) Characteristic friction coefficient and scale effects in oscillatory porous flow. Coast Eng 56(9):931–939. https://doi.org/10.1016/j.coastaleng.2009.05.002

Shih RS (2012) Experimental study on the performance characteristics of porous perpendicular pipe breakwaters. Ocean Eng 50:53–62. https://doi.org/10.1016/j.oceaneng.2012.05.010

Suh KD, Kim YW, Ji CH (2011) Calculation of permeability parameter of perforated wall. Coastal Engineering Proceedings 1(32):19. https://doi.org/10.9753/icce.v32.structures.19

Suh KD, Park JK, Park WS (2006) Wave reflection from partially perforated-wall caisson breakwater. Ocean Eng 33(2):264–280. https://doi.org/10.1016/j.oceaneng.2004.11.015

Teh HM, Venugopal V, Bruce T (2011) Hydrodynamic performance of a free surface semicircular perforated breakwater. Coastal Engineering Proceedings 1(32):20. https://doi.org/10.9753/icce.v32.structures.20

Teng B, Zhang XT, Ning DZ (2004) Interaction of oblique waves with infinite number of perforated caissons. Ocean Eng 31(5):615–632. https://doi.org/10.1016/j.oceaneng.2003.08.001

Thomson GG (2000) Wave transmission through multi-layered wave screens. *Queen's University, Kingston, Ontario,* Thomas Telford Publishing, Canada, 224

Zhu D (2011) Hydrodynamic characteristics of a single-row pile breakwater. Coast Eng 58(5):446–451. https://doi.org/10.1016/j.coastaleng.2011.01.003